ACS OMEGA

http://pubs.acs.org/journal/acsodf

Article

Open-Circuit Voltage (V_{OC}) Enhancement in TiO_2-Based DSSCs: Incorporation of ZnO Nanoflowers and Au Nanoparticles

Susana Borbón, Shadai Lugo, Dena Pourjafari, Nayely Pineda Aguilar, Gerko Oskam, and Israel López*

Cite This: *ACS Omega* 2020, 5, 10977−10986

Read Online

ACCESS | Metrics & More | Article Recommendations | Supporting Information

ABSTRACT: An important reason for the relatively low efficiency of dye-sensitized solar cells (DSSCs) is the low open-circuit voltage (V_{OC}) of about 0.7 V for a standard solar cell with a dye that has an absorption onset at 1.6 eV. We report an enhancement of the V_{OC} of about 0.10 V with respect to a TiO_2-based DSSC modified with ZnO nanoflowers that we prepared by a new and facile method. An additional increase of the V_{OC} of about 0.08 V was achieved by modifying the ZnO nanoflowers with Au nanoparticles, resulting in a DSSC with an efficiency of 2.79%, highlighted by a high V_{OC} of 0.89 V. Detailed analysis with electrochemical impedance spectroscopy and intensity-modulated photovoltage and photocurrent spectroscopies (IMVS and IMPS) reveal that the main reason for the increase of V_{OC} is related to the shift of the band edges upon coupling TiO_2 with ZnO nanoflowers, even though the electron lifetime at the same charge density actually decreases. These results show the intricate interplay between band edge shift, recombination kinetics, and DSSC performance and illustrate that a higher voltage DSSC can be fabricated by modification of the photoanode materials.

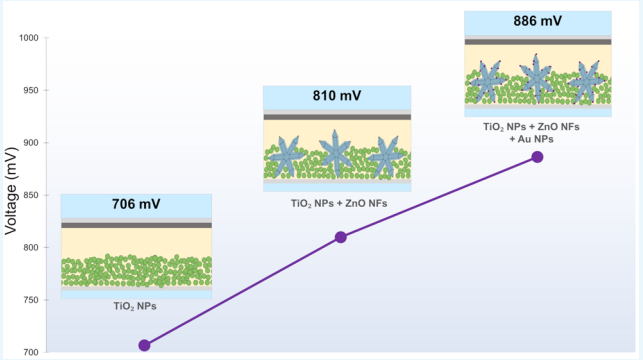

1. INTRODUCTION

Dye-sensitized solar cells (DSSCs) have been the center of attention for almost 3 decades after the report of Grätzel and O'Regan in 1991,[1] where they demonstrated the assembly of a DSSC based on TiO_2 nanoparticles that reached an efficiency of 7.1%. Their novel photovoltaic device consisted of a photoelectrochemical system based on working principles that are very different to the traditional silicon-based p−n junction solar cell.[2] The DSSCs have several advantages, such as a simple structure using nontoxic components, a potential for low-cost manufacturing processes, high efficiency even under diffuse light, and easy assembly on glass, metallic, and flexible substrates.[3−5] Figure 1 shows the structure of a DSSC and illustrates the main processes and general functioning of the cell. The energy levels of the materials have been reported by Wei et al.[6]

TiO_2 is the most used semiconductor in DSSC structure because of its properties such as wide band gap energy, high conduction band edge, large surface area, and excellent chemical stability. However, the electron mobility is quite low (0.1−4 cm^2/V s at 300 K) compared to other oxide semiconductors.[7] Different metal oxide semiconductors have been reported as an electron transport layer in DSSCs, such as ZnO,[8] SnO_2,[9] and Nb_2O_5,[10] with ZnO having the highest electron mobility (205−300 cm^2/V s at 300 K). Although the efficiency of ZnO-based DSSCs is still lower than that of TiO_2-based devices, ZnO can be considered an attractive alternative to TiO_2 because of its simple and low-cost synthesis methods.

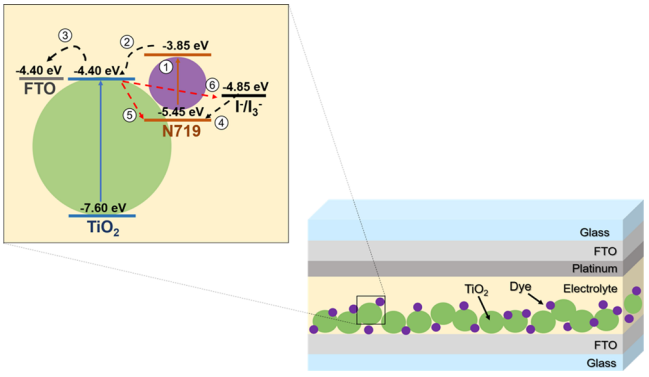

Figure 1. Scheme of a DSSC showing the architecture and its working principle with the energy levels: (1) light absorption by dye molecules and generation of an excited state, (2) electron injection from the dye into the semiconductor conduction band, (3) electron transport through the semiconductor to the back contact, (4) reduction of the oxidized dye molecule with iodide, resulting in regeneration of the dye ground state, and (5,6) electron recombination and recapture process by the dye and electrolyte, respectively.

Received: February 22, 2020
Accepted: April 27, 2020
Published: May 8, 2020

https://dx.doi.org/10.1021/acsomega.0c00794
ACS Omega 2020, 5, 10977−10986

Furthermore, it can be synthesized in a wide range of morphologies[7] including nanowires, nanotubes, nanotips, nanoforests, nanoflowers, nanosheets, and nanobelts.[11] Among all the different morphologies, ZnO nanoflowers have shown an enhancement in DSSC performance because of their larger surface area for dye adsorption, direct transport pathways, and efficient scattering centers for a better light harvesting efficiency.[12,13] The coupling of ZnO and TiO_2 has been investigated through different procedures such as simple addition of ZnO powder to TiO_2[14] or mixing both oxides during the synthesis process.[15,16] These procedures can result in a structure consisting of a blend of ZnO and TiO_2 nanoparticles or a core−shell structure.[17,18] ZnO nanoflowers have also been combined with TiO_2 using different strategies. Prabakar et al.[19] grew ZnO nanoflowers directly on fluorine-doped tin oxide (FTO) substrates using hexamethylenetetramine (HMTA) as an additive and coated them with TiO_2 using the sol−gel method, obtaining an efficiency of 3.1% and an increase of around 100 mV in open-circuit voltage (V_{OC}). Wei et al.[20] coupled TiO_2 nanoparticles and ZnO nanoflowers via a solution-phase method, controlling the morphology with HMTA. They achieved an efficiency of 2.82% using 25% of ZnO nanoflowers in the photoanode. Chauhan et al.[21] treated the surface of a ZnO nanoflower electrode with $TiCl_4$ in order to passivate the surface, resulting in an efficiency of 6.12%. They obtained the ZnO nanoflowers using a 24 h hydrothermal synthesis method without any additives to obtain the desired morphology. Even though the performance improvement in a TiO_2/ZnO nanoflower DSSC has already been shown, most of the reported devices require multistep synthesis methods, additives, or long reaction times to obtain ZnO nanoflowers or extra steps to fabricate the solar cell. These factors increase the fabrication cost and affect the large-scale production of the DSSC.

Recently, the incorporation of plasmonic metallic nanoparticles into the DSSC photoanode structure has been reported in order to improve the cell performance based on the localized surface plasmon resonance (LSPR).[22] There are various metal nanoparticles that have been incorporated, such as gold,[23] silver,[24] and aluminum;[25] gold and silver are the most common materials. Au nanoparticles have been incorporated in TiO_2-based[23,26] and ZnO-based photoanodes,[27] presenting in all cases an efficiency enhancement.

In this paper, we report on the assembly of a DSSC based on TiO_2 and ZnO nanoflowers, varying the proportion of ZnO in 5, 10, and 15%. The ZnO nanoflowers were synthesized using a solvothermal synthesis method in a conductively heated sealed vessel reactor, which allows shorter reaction times than conventional hydrothermal reactors. Besides a short reaction time, the absence of additives and extra steps in the cell assembly are other advantages of this strategy. In addition, the most efficient TiO_2/ZnO solar cell was further modified by adding different concentrations of Au nanoparticles in order to further enhance the device performance. Although a performance enhancement is often reported, a detailed explanation is often lacking. In this work, we use advanced electrochemical characterization techniques including electrochemical impedance spectroscopy (EIS) and intensity-modulated photovoltage and photocurrent spectroscopies (IMVS/IMPS) to determine the mechanisms behind the improved performance.

2. RESULTS AND DISCUSSION

2.1. ZnO Nanoflowers/TiO_2 Photoanode. Figure 2 shows a field emission scanning electron microscopy (FE-SEM) image of the synthesized ZnO nanomaterial, demonstrating a three-dimensional flower-like morphology, composed of six nanorods with pyramidal tips in the same plane and two nanorods perpendicular to the plane. The average width of the well-defined petals is 370 ± 50 nm, while the length is 772 ± 85 nm. The statistical average data were obtained measuring 50 nanoflowers using ImageJ software. The ZnO nanoflower material was blended with TiO_2 anatase nanoparticles in order to prepare the pastes denoted as 5Z, 10Z, and 15Z, where the number corresponds to the weight percentage of ZnO, and DSSCs were assembled and characterized.

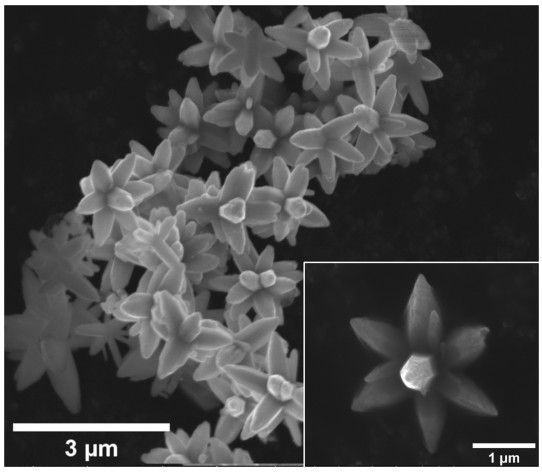

Figure 2. FE-SEM image of synthesized ZnO nanoflowers; the inset shows the high-magnification image of a nanoflower.

Figure 3 shows the XRD patterns of the screen-printed layers on the FTO substrate after sintering at 530 °C for T, 5Z, 10Z, and 15Z samples and the corresponding JCPDS for TiO_2, ZnO, and SnO_2. For all samples, the main peak corresponding to anatase (101) crystallographic plane at 25.28° is observed. For 5Z, 10Z, and 15Z samples, the reflections are consistent with the database pattern JCPDS no. 36-1451, which corresponds to ZnO in wurtzite phase, crystallized in

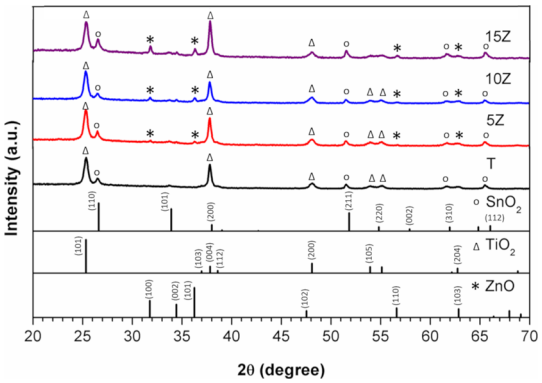

Figure 3. X-ray diffraction patterns of the printed layers of TiO_2 (T), 95% TiO_2/5% ZnO (5Z), 90% TiO_2/10% ZnO (10Z), and 85% TiO_2/15% ZnO (15Z) on FTO after sintering (JCPDS no. 21-1272 used for TiO_2 anatase, JCPDS no. 036-1451 for ZnO wurtzite, and JCPDS no. 41-14445 for SnO_2 cassiterite).

https://dx.doi.org/10.1021/acsomega.0c00794
ACS Omega 2020, 5, 10977−10986

hexagonal structure with spatial group $P6_3mc$. Furthermore, the peak intensity increases with the content of ZnO. Furthermore, diffraction peaks corresponding to SnO_2 in the cassiterite phase are observed in all samples; its presence is due to the FTO substrate.

Figure 4 shows the current density−voltage (J−V) curves of solar cells fabricated with the four different pastes. The curves

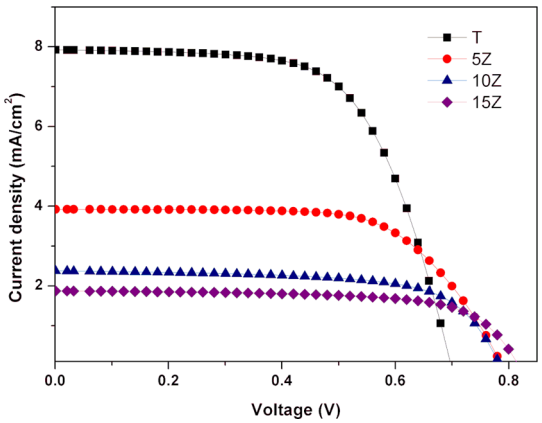

Figure 4. J−V curves of the samples T, 5Z, 10Z, and 15Z.

correspond to a cell with a performance close to the average values of the performance parameters, which are listed in Table 1.

The reference cells based on only TiO_2 show the best performance, achieving the highest short-circuit current density (J_{SC}). The efficiency of the Z-series cells based on TiO_2 mixed with ZnO nanoflowers decreases upon increasing the ZnO quantity, from 1.96% for 5Z cells to 1.20% for 15Z cells. On the other hand, the V_{OC} is higher for the solar cells with ZnO and is approximately the same for 5Z, 10Z, and 15Z; hence, the decrease in solar cell performance is mostly related to the decrease in J_{SC}, which decreases as the content of ZnO increases. Interestingly, J_{SC} drops approximately 50% for the photoanode with only 5% ZnO nanoflowers. There are several factors that influence the J_{SC}: (i) the amount of dye molecules adsorbed on the semiconductor surface that result in efficient light harvesting; (ii) the electron injection efficiency; (iii) the electron collection efficiency; and (iv) the dye regeneration efficiency.[28] Hence, several reports attribute lower J_{SC} values for ZnO-based DSSC to slower electron injection from dye to ZnO as compared to TiO_2, independently of the redox mediator used.[29] It has been noted that the electrical nature of ZnO, that is, its lower electric constant, does not facilitate the separation of charges in the interface of semiconductor/dye/electrolyte.[30] Furthermore, it is well known that ZnO is not stable under acidic conditions. In fact, the acidic N719 ethanolic solution has been shown to lead to the formation of Zn^{2+}−dye complexes that may hinder electron injection and block electron transport.[31] Moreover, as observed in Table 1, the relative surface area decreases considerably with the presence of ZnO nanoflowers. The higher surface area of sample T (107 m^2/g vs 70−73 m^2/g) allows for the adsorption of more dye molecules, which may directly improve the J_{SC}.

On the other hand, an important observation from Figure 4 and Table 1 is that the V_{OC} is approximately 100 mV larger for the cells containing ZnO as compared to TiO_2 cells. A large V_{OC} may be related to slow recombination and better electron collection efficiency. Hence, a possible explanation for the increase in V_{OC}, related to the incorporation of ZnO nanoflowers into the TiO_2 structure, may be the higher electron mobility of ZnO, which improves the electron transfer and facilitates the charge carrier separation.[32] According to the J−V curves, the fill factor (FF) for Z-series cells was slightly better than that for T cells. As is clear from this description, from only J−V curves, it is not possible to determine the fundamental reason for a change in performance. In order to distinguish between the different possible explanations, a detailed analysis needs to be performed using small-signal perturbation methods. EIS, IMPS, and IMVS are powerful tools to obtain quantitative information on the chemical capacitance (C_μ), the charge-transfer or recombination resistance (R_{ct} or R_{rec}), the electron lifetime, and the electron diffusion coefficient (D_n). For the systems under consideration here, we have compared the performance parameters of DSSCs consisting of TiO_2 modified with ZnO nanoflowers cells with those of only TiO_2 cells.

EIS measurements are generally performed under illumination at the voltage corresponding to open-circuit conditions; by varying the light intensity, the V_{OC} can be tuned and hence the quasi-Fermi level in the photoanode. EIS spectra were analyzed by fitting the results to the electrical circuit corresponding to the transmission line model developed by Bisquert et al.[33] using ZView software. The Nyquist plots related to each system are shown in Figure S1, and the corresponding electrical circuit is demonstrated in Figure S2, both in the Supporting Information. Interpretation of the impedance spectra using this model can provide direct information about the electron transport and recombination processes, charge accumulation, and the energetic distribution of trap states. Generally, the Nyquist plots have up to three semicircles, where the high-frequency semicircle is related to the charge-transfer resistance at the counter electrode (R_{Pt}), the medium-frequency semicircle is related to C_μ and the recombination resistance (R_{ct} or R_{rec}) at the interface between the semiconductor and the electrolyte, and the low-frequency semicircle is related to the diffusion impedance in the electrolyte (R_d); the low-frequency arc usually disappears in high-performance electrolytes, such as the I^-/I_3^- redox couple. The displacement from the origin corresponds to the series resistance, which is generally dominated by the FTO substrate resistance (R_s).[33]

Table 1. Photovoltaic Parameters and BET Surface Area of T, 5Z, 10Z, and 15Z Samples[a]

DSSC	BET (m^2/g)	V_{OC} (mV)	J_{SC} (mA/cm^2)	FF	η (%)
T	107	707 ± 11	7.20 ± 0.67	0.61 ± 0.01	3.12 ± 0.34
5Z	70	810 ± 14	3.68 ± 0.35	0.68 ± 0.04	1.96 ± 0.08
10Z	72	800 ± 0.0	2.74 ± 1.10	0.68 ± 0.02	1.49 ± 0.61
15Z	73	820 ± 0.0	2.12 ± 0.35	0.69 ± 0.01	1.20 ± 0.22

[a]The photovoltaic values correspond to the average of three measured cells or each series.

https://dx.doi.org/10.1021/acsomega.0c00794
ACS Omega 2020, 5, 10977−10986

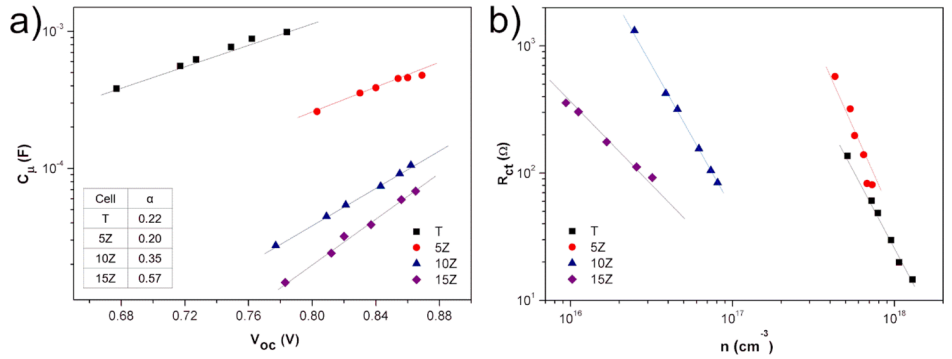

Figure 5. (a) Chemical capacitance, C_μ, vs the open-circuit voltage, V_{OC}, for the four systems. (b) Recombination resistance, R_{ct}, vs the total electron density, n, for the samples T, 5Z, 10Z, and 15Z.

The electrical circuit model was fitted to the Nyquist plots, which were obtained from the EIS spectra at each V_{OC}, and C_μ values were obtained from these fittings. Figure 5a shows C_μ as a function of V_{OC}, illustrating the typical exponential dependence in accordance with an exponential distribution of trap states characterized by the parameter, α, for all systems, as given in the general relation

$$C_\mu = \frac{q^2 N_T \alpha}{k_B T}\exp\left(-\frac{\alpha(E_c - E_{redox})}{k_B T}\right)\exp\left(\frac{\alpha q V_{OC}}{k_B T}\right) = C_0 \exp\left(\frac{\alpha q V_{OC}}{k_B T}\right) \quad (1)$$

Equation 1 shows that, through the value of C_0, the value of C_μ also depends on the total density of traps, N_T, and the position of the conduction band edge of the semiconductor material with respect to the redox energy, $(E_C - E_{redox})$; hence, C_0 may be different for the different photoanode materials. For all cells, C_μ increases when V_{OC} increases. It can be observed that there is a significant difference both in C_μ values and the slopes of the graphs, specifically between the T and 5Z cells and between the 10Z and 15Z cells. These results indicate that the systems have different trap distributions.

In addition, Figure 5a shows that the values of C_μ are markedly different for the systems with more ZnO, which is caused by a lower density of trap states at the respective quasi-Fermi level. This behavior is either due to a lower intrinsic trap density or because of a shift of the band edges to higher energy. Since for all systems the majority material is TiO_2, it is more likely that a significant shift of the band edges, due to charging of the ZnO component, is responsible for these observations. The shift of the band edges to higher energy strongly affects the cell performance: on the one hand, V_{OC} may increase but, on the other hand, the injection efficiency may decrease. The magnitude of the shift increases with the amount of ZnO; thus, it is likely that an optimal amount of ZnO exists where the cell performance is better. Hence, the EIS measurements indicate that there is a significant shift of the band edges, which results in a lower injection efficiency deriving in a lower J_{SC} and also in an increase in V_{OC}. Interestingly, the shift of the band edges increases strongly with the amount of ZnO; however, V_{OC} increases significantly for the 5Z samples but then appears to saturate.

The charge at a given open-circuit voltage is expressed as $dn = C_\mu dV_{OC}$, and, hence, the total charge, n, can be obtained as a function of voltage by integration of eq 1, which results in the following equation

$$n(V_{OC}) = \frac{k_B T}{\alpha q} C_0 \exp\left(\frac{\alpha q V_{OC}}{k_B T}\right) = \frac{k_B T}{\alpha q} C_\mu \quad (2)$$

Equation 2 indicates that C_μ is linear with electron density. This can be seen as a straight line with a slope of 1 and an intercept of α in Figure S3 (Supporting Information), where C_μ is graphed versus the total electron density in a log−log plot.

In order to determine the effect of recombination kinetics on the cell performance, it is useful to plot R_{ct} versus n as determined from C_μ, which is shown in Figure 5b.

The recombination resistance decreases with increasing electron density, indicating that recombination becomes faster in agreement with expectations. In addition, it can be observed that R_{ct} at a fixed total electron density is much larger for the T and 5Z cells than for the 10Z and 15Z cells that have more ZnO, suggesting that recombination is faster at the ZnO surface, which is in agreement with previous studies. As a consequence, it can be inferred that the V_{OC} for the 10Z and 15Z samples saturates because of faster recombination kinetics, off-setting the benefits of the band edge shift.

This interpretation can be corroborated by evaluating the electron lifetime as a function of electron density, that is, the quasi-Fermi level. The lifetime can be obtained from both EIS and IMVS, which are also conducted under open-circuit conditions. From EIS, the electron lifetime is calculated from $\tau_n = R_{ct} C_\mu$. The IMVS spectra generally consist of a single semicircle, and the lifetime is obtained from the frequency at the apex using $\tau_{IMVS} = 1/\omega_{min}$. Figure S4, in the Supporting Information, shows a representative IMVS spectrum. Figure 6 shows the electron lifetime versus the electron density for the four systems, and it can be observed that EIS and IMVS give very similar results. In addition, the lifetime follows the same trends as observed for R_{ct}, thus corroborating the results.

The recombination kinetics as described by the lifetime, combined with the relative position of the band edges, determine the open-circuit conditions; however, electron transport may also play an important role, in particular in the collection efficiency: faster transport may compete more successfully with recombination. IMPS is performed under short-circuit conditions, and the transport time constant can be obtained from the apex of the single arc. The arc is usually observed through $\tau_{IMPS} = 1/\omega_{min} = d^2/\gamma D_n$, where D_n is the effective electron diffusion coefficient, d is the film thickness, and γ is a constant that is taken to be 2.35, as generally observed for TiO_2.[34] Figure S5, in the Supporting Information, shows a representative IMPS spectrum. Figure 7 shows the

https://dx.doi.org/10.1021/acsomega.0c00794
ACS Omega 2020, 5, 10977−10986

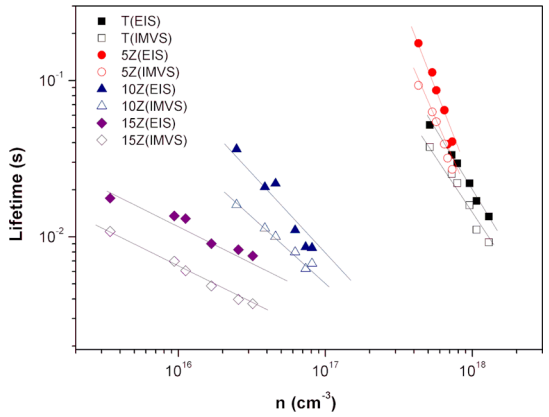

Figure 6. Electron lifetime vs the total electron, *n*, density for samples T, 5Z, 10Z, and 15Z obtained from both EIS and IMVS under open-circuit conditions.

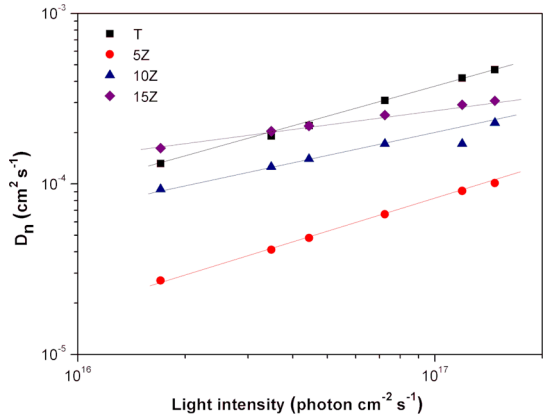

Figure 7. Electron diffusion coefficient (D_n) vs incident light intensity for T, 5Z, 10Z, and 15Z solar cells obtained from IMPS measurements under short-circuit conditions.

dependence of D_n obtained under short-circuit conditions on the light intensity, illustrating the exponential dependence characteristic of trap-limited transport. In this case, it is observed that the T samples have the best transport properties and that the 10Z and 15Z samples show a very similar behavior; transport is slightly slower for the 5Z cells. It should be stressed that if the injection efficiency is different between the T and Z cells, as concluded from the *J*−*V* curves and EIS results under open-circuit conditions, the total electron density in the films is not the same for the different samples at the same photon flux. This complicates a precise interpretation of these results; however, the T cells have a higher injection efficiency, which explains the higher D_n with respect to the 5Z cells. In general, these results indicate that the transport properties do not significantly affect cell performance but rather that recombination and shift of the band edges govern the performance.

2.2. Incorporation of Plasmonic Au Nanoparticles on Flower-like ZnO Particles. Because the 5Z cells have shown the best performance among the Z-series cells, this ZnO proportion (5%) was selected for the incorporation of Au nanoparticles. The concentration of Au nanoparticles added into the DSSC was varied to evaluate its effect on device performance. Figure 8 shows FE-SEM images of the flower-like ZnO/Au nanostructures. In these micrographs, the Au nanoparticles are well distributed over the structure without

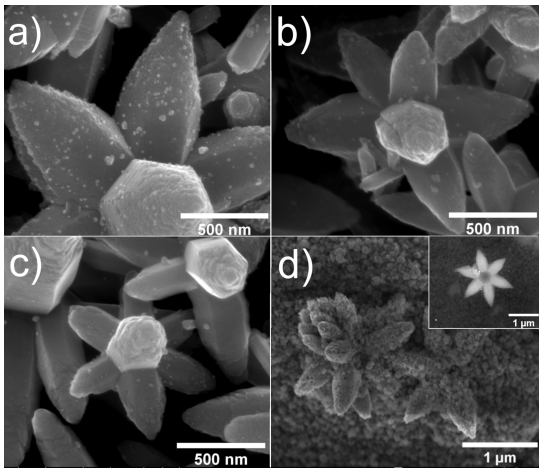

Figure 8. FE-SEM images of flower-like ZnO/Au nanostructures with a varying quantity of Au nanoparticles in samples: (a) 12,020; (b) 11,000; and (c) 8360 mg/kg; (d) FE-SEM image of the DSSC electrode 5Z consisting of 95% TiO_2 and 5% ZnO; inset: FE-SEM image of the photoanode 5Z-601A.

forming agglomerates, as confirmed by elemental X-ray Au maps (Figures S6−S8 in the Supporting Information). The Au nanoparticle size is 26 ± 5 nm for sample 5Z-601A, 17 ± 3 nm for sample 5Z-550A, and 14 ± 2 nm for sample 5Z-418A. The average size and standard deviation of the Au nanoparticles were obtained using ImageJ software based on the measurement of 50 nanoparticles. As the quantity of Au decreases, the particle size also decreases, which is due to the synthesis method: as the relative quantity of ZnO powder in the reaction increases, the concentration of precursors ($HAuCl_4$ and sodium citrate) decreases, leading to smaller nanoparticles. The elemental composition was determined by energy-dispersive X-ray spectroscopy (EDXS) (Figure S9 in the Supporting Information), and the presence of Zn, O, and Au with well-defined peaks is confirmed; no other peaks corresponding to impurities were detected.

In order to assess the chemical composition, the ZnO/Au samples were analyzed by inductively coupled plasma atomic emission spectroscopy (ICP-AES). The Au concentration values (experimental composition) are about 12,020, 11,000, and 8360 mg/kg (ppm). Therefore, the final experimental concentration of Au in the TiO_2/ZnO/Au composites is as follows: 601, 550, and 418 mg/kg (ppm) for samples 5Z-601A, 5Z-550A, and 5Z-418A, respectively. The last three digits of the name of each sample correspond to the ppm value of Au present in the photoanode. Figure 8d shows representative FE-SEM images of the screen-printed photoanode (5Z sample), and the inset shows the TiO_2/ZnO/Au composite for the 5Z-601A sample as an example.

DSSCs have been fabricated with the three different pastes containing 95% TiO_2 and 5% ZnO, with the ZnO decorated with different quantities of Au nanoparticles. Figure 9 shows the *J*−*V* curves of cells with photovoltaic performance close to the average performance, as detailed in Table 2. The incorporation of Au nanoparticles affects both the J_{SC} and V_{OC} values of the solar cells, depending on the concentration of particles added to the system. For all cells, a further increase in the V_{OC} was observed as compared to the reference cell (5Z).

The influence of the incorporation of plasmonic nanoparticles on the performance of DSSC has been reported

https://dx.doi.org/10.1021/acsomega.0c00794
ACS Omega 2020, 5, 10977−10986

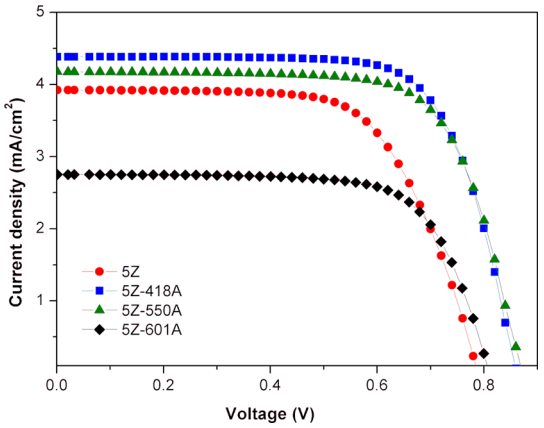

Figure 9. $J-V$ curves of solar cells 5Z, 5Z-418A, 5Z-550A, and 5Z-601A.

Table 2. Photovoltaic Parameters of Samples 5Z, 5Z-418A, 5Z-550A, and 5Z-601A[a]

DSSC	V_{OC} (mV)	J_{SC} (mA/cm^2)	FF	η (%)
5Z	810 ± 14	3.68 ± 0.35	0.68 ± 0.04	1.96 ± 0.08
5Z-418A	886 ± 11	4.55 ± 0.43	0.73 ± 0.01	2.79 ± 0.25
5Z-550A	867 ± 23	4.02 ± 0.14	0.70 ± 0.03	2.38 ± 0.19
5Z-601A	813 ± 12	2.91 ± 0.74	0.69 ± 0.03	1.62 ± 0.33

[a]The values are for three measured cells for each series and their corresponding standard deviations.

previously and in general has been ascribed to a combination of effects. A shift in a semiconductor quasi-Fermi level to more negative potential values may occur due to electron storage and equilibration between the metal oxide and the metallic nanoparticles[35,36] and, as a result, the V_{OC} may increase.[37,38] According to Figure 9 and Table 2, the V_{OC} increased approximately 3, 57, and 77 mV for 5Z-601, 5Z-550, and 5Z-418 systems, respectively. It has been shown that the beneficial effect of the presence of plasmonic nanoparticles not only depends on particle size but also on the quantity.[39,40] For example, the V_{OC} of 5Z-601 samples with the largest Au particles in both size and quantity was slightly (only 3 mv) higher than the V_{OC} of 5Z cells. This has been attributed to plasmonic nanoparticles acting as recombination centers when their quantity increases.[25,37,39] Recent research suggests that this phenomenon does not fully explain the dependence of performance on nanoparticle density and size.[41]

The effect of Au nanoparticle size and quantity on J_{SC} shows a similar tendency: for the larger nanoparticles and larger quantity, J_{SC} in fact decreases compared to the neat 5Z solar cell, while for the smaller nanoparticles at smaller quantities, J_{SC} increases. The enhancement of J_{SC} is generally ascribed to improved light harvesting, related to both LSPR effects allowing for more efficient light absorption by the dye and the optical absorption of the plasmonic nanoparticles.[39,41] Moreover, a shift of the band edges related with the trapping of charge on the nanoparticles may also affect the injection efficiency for large concentration of Au nanoparticles.[42,43]

For a detailed analysis of the systems under study, EIS, IMPS, and IMVS were performed to obtain quantitative information on the C_μ, R_{ct}, electron lifetime, and D_n. The EIS spectra of the DSSC with different concentrations of Au nanoparticles are shown in Figure S10 (Supporting Information). Figure 10 shows C_μ and R_{ct} versus V_{OC} and n, respectively, for the different systems. From Figure 10a, it can be concluded that the trap distribution parameter, obtained from the slope of the curves, is approximately the same for all the three systems with Au nanoparticles, although it is slightly larger than that for 5Z solar cells without Au. In addition, it can be seen that the curves are shifted to the right, to larger potentials, which indicates that the incorporation of Au nanoparticles leads to a shift of the band edges under illumination. Therefore, these results indicate that the increase of V_{OC} for cells with Au nanoparticles is partially caused by a further shift of the band edges to higher energies.

The influence of the plasmonic Au nanoparticles on the recombination kinetics can be evaluated from Figure 10b, which shows that R_{ct} at the same charge density depends on the size and concentration of Au nanoparticles. In general, it can be seen that R_{ct} is smaller at the same value of the electron density when Au nanoparticles are present, decreasing with increasing concentration and size. This indicates that the charge-transfer process corresponding to recombination becomes faster upon incorporation of Au. Also, in this case, the slope of the curves is the same for the cells with plasmonic Au nanoparticles. These results clearly indicate that although a larger V_{OC} is obtained upon incorporating Au nanoparticles, this is not due to a decrease of the recombination kinetics but rather to a shift of the band edges.

This can be further evaluated by plotting the electron lifetime versus the total electron density, which is shown in Figure 11. It can be seen that the lifetime follows the same trends as R_{ct}, indicating that recombination is effectively faster

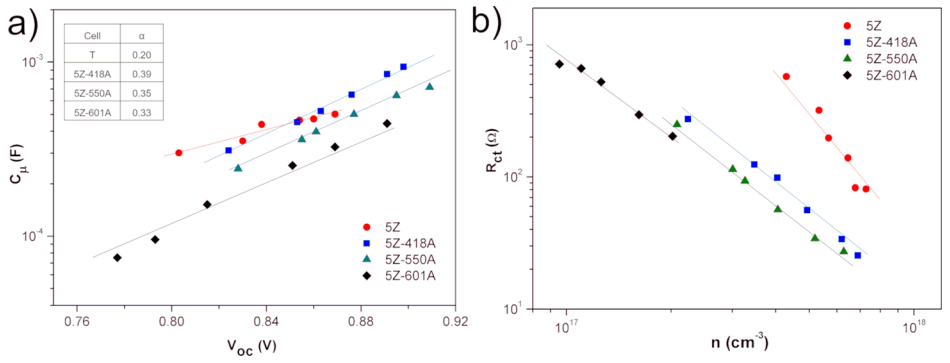

Figure 10. (a) Chemical capacitance, C_μ, vs open-circuit voltage, V_{OC}, and (b) R_{ct} vs total electron density, n, obtained from EIS measurements under open-circuit conditions for samples 5Z, 5Z-601A, 5Z-550A, and 5Z-418A, where the value of n is controlled by tuning the light intensity.

https://dx.doi.org/10.1021/acsomega.0c00794
ACS Omega 2020, 5, 10977−10986

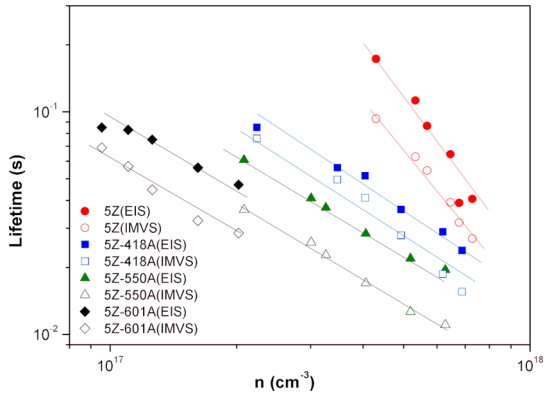

Figure 11. Electron lifetime obtained from EIS and IMVS performed under open-circuit conditions vs total electron density, n, for the samples 5Z, 5Z-601A, 5Z-550A, and 5Z-418A, respectively.

in the presence of Au nanoparticles, if compared at the same electron density. However, thanks to the shift of the band edges to higher energy, the electron density is reached at larger values of V_{OC}, thus resulting in improved performance of the DSSC. The IMVS spectra are shown in Figure S11 in the Supporting Information.

The effect of the presence of plasmonic Au nanoparticles on the electron transport kinetics was evaluated using IMPS under short-circuit conditions; see Figure S12 (Supporting Information) for the IMPS spectra. Figure 12 shows D_n versus the light intensity, and it can be concluded that D_n increases in the presence of Au nanoparticles, following a similar trend as J_{SC}.

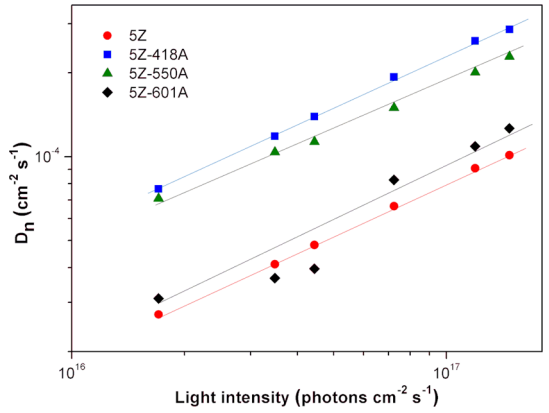

Figure 12. Electron diffusion length vs incident light intensity for DSSC samples 5Z, 5Z-601A, 5Z-550A, and 5Z-418A obtained from IMPS measurements under short-circuit conditions.

These results imply that the increase in D_n may be related to the increase in electron density in the semiconductor material because of LSPR promoted by the Au nanoparticles. The plasmonic nanoparticles store some of the electrons (photocharging effect) and change the Fermi level of the semiconductor. This follows a similar fashion as the one observed for the dependence of the D_n on the quantity of ZnO nanoflowers present in the photoanode. It can be concluded that the quantity of Au nanoparticles is crucial and provides means to further optimize the performance of DSSC.

3. CONCLUSIONS

The influence of the incorporation of ZnO nanoflowers into the photoanode nanomaterial on the performance of TiO_2-based DSSC has been evaluated in detail using both standard and specialized small-signal modulation methods, EIS, and IMVS/IMPS. In addition, the effect of modifying the ZnO nanoflowers with plasmonic Au nanoparticles has been determined.

The incorporation of ZnO nanoflowers results in a decrease of J_{SC}; however, the V_{OC} increases significantly as compared to TiO_2-based solar cells by up to 100 mV. These results are consistent with an interpretation where the band edges shift to higher energy upon adding ZnO related to trapped charge in the ZnO nanoflowers. Consequently, the injection efficiency and, hence, the J_{SC} decreases, but the maximum attainable V_{OC} increases. EIS, IMVS, and IMPS measurements confirm the shift of the band edges and show that although the recombination at the same electron density is, in fact, faster in the presence of ZnO, the benefits of the band edge shift for the V_{OC} can still be obtained. The best performing proportion of ZnO is found to be 5%; upon further addition, the injection efficiency decreases even more, and the J_{SC} becomes too small. The incorporation of ZnO is shown not to affect the transport kinetics significantly, as the effective electron diffusion coefficient, D_n, is only weakly affected by the addition of ZnO.

For the best performing proportion of ZnO nanoflowers (5%), the material was further modified with plasmonic Au nanoparticles. In this case, both the J_{SC} and V_{OC} increase at the most fitting concentration of Au nanoparticles. The increase in J_{SC} is related to the positive effect of the presence of plasmonic Au nanoparticles on the overall absorption of light by the dye. In addition, the extra charge on the Au nanoparticles results in an additional shift of the band edges, which translates into a further increase of the V_{OC}. Also, in this case, the concentration of Au nanoparticles is important: when more Au is added, both the current and the voltage decrease because of faster recombination kinetics, resulting in a reduction of light harvesting efficiency. The faster recombination kinetics is clearly observed in the results from EIS and IMVS that show that the electron lifetime decreases dramatically upon adding more Au. The value of D_n increases when more Au nanoparticles are added to the system; however, this improvement cannot offset the negative effects of faster recombination.

The most efficient device, among the DSSC with incorporation of ZnO–Au into a TiO_2 photoanode, consists of 5% of ZnO, 95% of TiO_2, and 418 ppm of Au nanoparticles, achieving an efficiency of 2.8%, which is still slightly lower than for only TiO_2 at 3.1%. However, the V_{OC} obtained is much larger at 0.89 V as compared to 0.71 V, indicating that the Au-modified TiO_2/ZnO composite photoanode provides a promising alternative for the supply of higher voltage. In order to increase the photocurrent, a change in the dye chemistry may provide a further improvement of the solar cell performance.

4. EXPERIMENTAL DETAILS

4.1. ZnO Nanoflowers and Decoration with Au Nanoparticles. The hydrothermal synthesis of ZnO nanoflowers was carried out at 140 °C for 30 min in a conductively heated sealed vessel reactor (Monowave 50, Anton Paar) as previously reported.[44] The morphology of the ZnO nano-

https://dx.doi.org/10.1021/acsomega.0c00794
ACS Omega 2020, 5, 10977−10986

flowers was analyzed using a field emission scanning electron microscope(FEI Nova NanoSEM 200).

ZnO nanoflowers were decorated with Au nanoparticles using 0.0102, 0.0204, and 0.0305 g of ZnO nanoflowers in 10 mL of 0.25 mM $HAuCl_4$ solution (Aldrich, hydrogen tetrachloroaurate trihydrate ≥99%). The dispersions were heated to the boiling point under magnetic stirring. At the boiling temperature (100 °C), 500 μL of 1% wt/v sodium citrate dihydrate (Aldrich, $Na_3C_6H_5O_7{\cdot}2H_2O$ ≥ 99%, FG) solution was added and the dispersions were maintained at the boiling temperature under stirring for 20 min. The dispersions were centrifuged and washed with distilled water and then dried at 100 °C for 2 h. The morphology of the flower-like ZnO/Au nanocomposites was observed by FE-SEM, using a Helix detector. The elemental composition was determined by EDXS using an INCA X-Sight EDS detector coupled to the microscope. To measure the concentration of Au in the ZnO/Au mixtures, ICP-AES was performed employing a Thermo Electron-ICAP 6500. For the preparation of the samples, 21 mg of each ZnO/Au mixture was dissolved in 12 mL of aqua regia (HCl/HNO_3—3:1). The acid digestion process was carried out in an open vessel on a hot plate (70−85 °C).

4.2. Semiconductor Paste Preparation. The screen-printing pastes were prepared using two solutions: (1) 0.15 g of ethyl cellulose (Aldrich, 100 cP) in 10 mL of ethanol and (2) 0.5 g of synthesized powder in 10 mL of ethanol. Both solutions were sonicated separately. After a 1 h sonication, 4.1 g of terpineol (Aldrich 99.5%, mixture of isomers, anhydrous) was added to solution (2), followed by another 1 h sonication. Then, solution (1) was added to the suspension and the mixture was sonicated for 1 h. The excess ethanol was removed with a rotary evaporator (Buchi R-210), resulting in seven different pastes, including only TiO_2 nanoparticles (Aldrich, nanopowder <25 nm, 99.7%) as reference cells (T) and TiO_2/ZnO blends of 5, 10, and 15% of ZnO nanoflowers in TiO_2 structure, labeled 5Z, 10Z, and 15Z-series cells, respectively. Nitrogen adsorption/desorption isotherms were obtained with a surface analyzer BELSORP max II (BELSORP series, BEL Japan, Inc), and through the Brunauer−Emmett−Teller (BET) method, the surface area was calculated. As will be explained later, the 5:95 ZnO nanoflower/TiO_2 nanoparticle composite was used for the experiments where the material was decorated with Au nanoparticles. Using the same procedure, other pastes were prepared with different proportions of Au nanoparticles for the 5:95 ZnO nanoflower/TiO_2 nanoparticle composite, which are identified as 5Z-601A, 5Z-550A, and 5Z-418A.

4.3. Solar Cell Assembly. FTO on glass with a sheet resistance of 15 and 8 Ω/□ was used for the working and counter electrodes, respectively (TEC 15 and TEC 8; Xop Glass). The FTO substrates were sequentially cleaned in an ultrasonic bath of distilled water, ethanol, and isopropyl alcohol for 20 min, followed by drying in air. The working electrodes were prepared by the deposition of different pastes on TEC 15 using screen-printing (ATMA, AT-25PA, a digital electric flat screen printer). To obtain a final thickness of about 11 μm, several layers (between 7 and 11) were deposited in an area of 0.5 cm^2 with 10 min of heat treatment at 120 °C between each layer. When the desired thickness was reached, the substrates were sintered at 530 °C for 1 h to eliminate the organic binder. The final thickness was measured after sintering using a profilometer (KLA-Tencor AlphaStep D-120). The substrates at 80 °C were immersed in a 0.3 mM ethanolic solution of N719 dye (Dyesol) for 24 h. The sensitized substrates were rinsed with ethanol to eliminate any excess of dye molecules.

For the counter electrodes, two small electrolyte-filling holes were drilled in TEC 8 substrates before cleaning. The substrates were then masked to obtain the same area as the corresponding active area on the working electrodes (0.5 cm^2), and a drop of Platisol T (Solaronix) solution was brushed onto the exposed area. The substrates were heated to 450 °C for 10 min, resulting in formation of a thin platinum film.

The two electrodes (working and counter) were assembled into a sandwich-type cell using the thermoplastic Surlyn (70 μm) as the sealing material; the cells were sealed in an oven at 215 °C for 100 s. The electrolyte solution was injected through the holes in the counter electrode. The electrolyte consisted of 0.1 M LiI (Aldrich, 99.9%), 0.1 M GuSCN (Aldrich, ≥97%), 0.05 M I_2 (Aldrich, ≥99.8), 0.5 M 4-*tert*-butylpyridine (TBP, Aldrich 96%), and 0.6 M 1,2-dimethyl-3-propylimidazolium iodide (DMPII, Solaronix) in a mixture of acetonitrile (Aldrich, 99.8%) and valeronitrile (Aldrich, 99.5%) (85:15 v/v). The holes were sealed using Surlyn and a microscope cover glass slide. The conductive side of the FTO substrates was painted with a conductive silver paint (SPI Supplies) to improve the external contact. For each paste, three solar cells were fabricated in order to confirm the reproducibility of the fabrication process and the results from the electrochemical analysis.

4.4. DSSC Characterization. The crystalline structure of the semiconductor oxide in the electrodes was obtained by X-ray diffraction analysis using a Siemens D-5000 diffractometer at room temperature with Cu Kα radiation (1.5405 Å) within a Bragg angle 2θ range from 20 to 80°.

Photovoltaic characterization was carried out using a setup consisting of a 450 W ozone-free Xe-lamp (Newport Corporation) with a 10 cm water filter and an AM 1.5 G optical filter (Newport Corporation) calibrated to an irradiance of 100 mW/cm^2 using a certified 4 cm^2 monocrystalline silicon reference cell with an incorporated KG-5 filter. The $J-V$ curves were obtained using a Gamry ZRA 3000 potentiostat/galvanostat. EIS, IMVS, and IMPS were performed with an Autolab PGSTAT302N/FRA2 setup, and NOVA 2.1 software was used for data acquisition. The EIS spectra were obtained under red light-emitting diode (LED) illumination (625 nm) using an ac amplitude of 10 mV in the frequency range from 0.1 to 100 kHz. EIS measurements were performed at the V_{OC}, which was varied using neutral density filters mounted in a filter wheel. IMPS and IMVS measurements were performed at modulation frequencies between 1 mHz and 10 kHz. A red LED (625 nm) was used to illuminate the samples. The EIS, IMVS, and IMPS results were analyzed using ZView software.

■ ASSOCIATED CONTENT

Supporting Information

The Supporting Information is available free of charge at https://pubs.acs.org/doi/10.1021/acsomega.0c00794.

Nyquist plots of all the DSSCs, equivalent circuit used for the interpretation of EIS spectra, chemical capacitance versus total electron density plots, IMVS and IMPS spectra, FE-SEM images and elemental Au mapping of ZnO/Au nanoflowers, and EDXS spectra of ZnO/Au nanoflowers (PDF)

https://dx.doi.org/10.1021/acsomega.0c00794
ACS Omega 2020, 5, 10977−10986

AUTHOR INFORMATION

Corresponding Author

Israel López − *Universidad Autónoma de Nuevo León, UANL, Centro de Investigación en Biotecnología y Nanotecnología (CIBYN), Laboratorio de Nanociencias y Nanotecnología and Facultad de Ciencias Químicas, Laboratorio de Materiales I, 66629 Apodaca, Nuevo León, Mexico;* orcid.org/0000-0002-0957-3062; Phone: +52 (81) 8329 4000 ext. 4202; Email: israel.lopezhr@uanl.edu.mx

Authors

Susana Borbón − *Universidad Autónoma de Nuevo León, UANL, Centro de Investigación en Biotecnología y Nanotecnología (CIBYN), Laboratorio de Nanociencias y Nanotecnología and Facultad de Ciencias Químicas, Laboratorio de Materiales I, 66629 Apodaca, Nuevo León, Mexico*

Shadai Lugo − *Universidad Autónoma de Nuevo León, UANL, Facultad de Ciencias Químicas, 64570 Monterrey, Nuevo León, Mexico*

Dena Pourjafari − *Centro de Investigación y de Estudios Avanzados del IPN (CINVESTAV), Departamento de Facísica Aplicada, 97310 Mérida, Yucatán, Mexico;* orcid.org/0000-0002-0008-4609

Nayely Pineda Aguilar − *Centro de Investigación en Materiales Avanzados, S. C. (CIMAV), 66628 Apodaca, Nuevo León, Mexico*

Gerko Oskam − *Centro de Investigación y de Estudios Avanzados del IPN (CINVESTAV), Departamento de Facísica Aplicada, 97310 Mérida, Yucatán, Mexico;* orcid.org/0000-0002-2105-5874

Complete contact information is available at: https://pubs.acs.org/10.1021/acsomega.0c00794

Notes

The authors declare no competing financial interest.

ACKNOWLEDGMENTS

The authors acknowledge the Consejo Nacional de Ciencia y Tecnologia of Mexico (CONACYT) for the M. Sc. research scholarship of S.B. (487884). Also, CONACYT is acknowledged for funding under projects CB-178510 and CB-A1-S-21018.

REFERENCES

(1) O'Regan, B.; Grätzel, M. A low-cost, high-efficiency solar-cell based on dye-sensitized colloidal TiO_2 films. *Nature* **1991**, *353*, 737−740.

(2) Kayes, B. M.; Atwater, H. A.; Lewis, N. S. Comparison of the device physics principles of planar and radial p-n junction nanorod solar cells. *J. Appl. Phys.* **2005**, *97*, 114302.

(3) Hug, H.; Bader, M.; Mair, P.; Glatzel, T. Biophotovoltaics: Natural pigments in dye-sensitized solar cells. *Appl. Energy* **2014**, *115*, 216−225.

(4) Sharma, S.; Bulkesh Siwach, S.; Ghoshal, S. K.; Mohan, D. Dye sensitized solar cells: From genesis to recent drifts. *Renewable Sustainable Energy Rev.* **2017**, *70*, 529−537.

(5) Ye, M.; Wen, X.; Wang, M.; Iocozzia, J.; Zhang, N.; Lin, C.; Lin, Z. Recent advances in dye-sensitized solar cells: From photoanodes, sensitizers and electrolytes to counter electrodes. *Mater. Today* **2015**, *18*, 155−162.

(6) Wei, L.; Yang, Y.; Fan, R.; Wang, P.; Li, L.; Yu, J.; Yang, B.; Cao, W. Enhance the performance of dye-sensitized solar cells by co-sensitization of 2,6-bis(iminoalkyl)pyridine and N719. *RSC Adv.* **2013**, *3*, 25908−25916.

(7) Zhang, Q.; Dandeneau, C. S.; Zhou, X.; Cao, G. ZnO nanostructures for dye-sensitized solar cells. *Adv. Mater.* **2009**, *21*, 4087−4108.

(8) Karst, N.; Rey, G.; Doisneau, B.; Roussel, H.; Deshayes, R.; Consonni, V.; Ternon, C.; Bellet, D. Fabrication and characterization of a composite ZnO semiconductor as electron transporting layer in dye-sensitized solar cells. *Mater. Sci. Eng. B Solid State Mater. Adv. Technol.* **2011**, *176*, 653−659.

(9) Snaith, H. J.; Ducati, C. SnO_2-Based dye-sensitized hybrid solar cells exhibiting near unity absorbed photon-to-electron conversion efficiency. *Nano Lett.* **2010**, *10*, 1259−1265.

(10) Ou, J. Z.; Rani, R. A.; Ham, M.-H.; Field, M. R.; Zhang, Y.; Zheng, H.; Reece, P.; Zhuiykov, S.; Sriram, S.; Bhaskaran, M.; Kaner, R. B.; Kalantar-Zadeh, K. Elevated temperature anodized Nb_2O_5: A photoanode material with exceptionally large photoconversion efficiencies. *ACS Nano* **2012**, *6*, 4045−4053.

(11) Lizama-Tzec, F. I.; García-Rodríguez, R.; Rodríguez-Gattorno, G.; Canto-Aguilar, E. J.; Vega-Poot, A. G.; Heredia-Cervera, B. E.; Villanueva-Cab, J.; Morales-Flores, N.; Pal, U.; Oskam, G. Influence of morphology on the performance of ZnO-based dye-sensitized solar cells. *RSC Adv.* **2016**, *6*, 37424−37433.

(12) Omar, A.; Abdullah, H. Electron transport analysis in zinc oxide-based dye-sensitized solar cells: A review. *Renewable Sustainable Energy Rev.* **2014**, *31*, 149−157.

(13) Kilic, B.; Günes, T.; Besirli, I.; Sezginer, M.; Tuzemen, S. Construction of 3-dimensional ZnO-nanoflower structures for high quantum and photocurrent efficiency in dye sensitized solar cell. *Appl. Surf. Sci.* **2014**, *318*, 32−36.

(14) Chamanzadeh, Z.; Noormohammadi, M.; Zahedifar, M. Enhanced photovoltaic performance of dye sensitized solar cell using TiO_2 and ZnO nanoparticles on top of free standing TiO_2 nanotube arrays. *Mater. Sci. Semicond. Process.* **2017**, *61*, 107−113.

(15) Aliah, H.; Bernando, B.; Puspitasari, F.; Setiawan, A.; Pitriana, P.; Nuryadin, B. W.; Ramdhani, M. A. Dye sensitized solar cells (DSSC) performance reviewed from the composition of titanium dioxide (TiO_2)/zinc oxide (ZnO). *IOP Conf. Ser.: Mater. Sci. Eng.* **2018**, *288*, 012070.

(16) Boro, B.; Gogoi, B.; Rajbongshi, B. M.; Ramchiary, A. Nano-structured TiO_2/ZnO nanocomposite for dye-sensitized solar cells application: A review. *Renewable Sustainable Energy Rev.* **2018**, *81*, 2264−2270.

(17) Karam, C.; Habchi, R.; Tingry, S.; Miele, P.; Bechelany, M. Design of multilayers of urchin-like ZnO nanowires coated with TiO_2 nanostructures for dye-sensitized solar cells. *ACS Appl. Nano Mater.* **2018**, *1*, 3705−3714.

(18) Khan, M. I.; Saleem, M.; Rehman, S. U.; Ali, S. S.; Qadri, M. U. Stacked layer effect of ZnO/TiO_2 on the efficiency of dye sensitized solar cells. *J. Nanoelectron. Optoelectron.* **2019**, *14*, 291−296.

(19) Prabakar, K.; Son, M.; Kim, W.-Y.; Kim, H. TiO_2 thin film encapsulated ZnO nanorod and nanoflower dye sensitized solar cells. *Mater. Chem. Phys.* **2011**, *125*, 12−14.

(20) Liu, J.; Wei, A.; Zhao, Y.; Lin, K.; Luo, F. Dye-sensitized solar cells based on ZnO nanoflowers and TiO_2 nanoparticles composite photoanodes. *J. Mater. Sci.: Mater. Electron.* **2014**, *25*, 1122−1126.

(21) Waghadkar, Y.; Shinde, M.; Rane, S.; Gosavi, S.; Terashima, C.; Fujishima, A.; Chauhan, R. Highly efficient dye-sensitized solar cells by $TiCl_4$ surface modification of ZnO nano-flower thin film. *J. Solid State Electrochem.* **2018**, *22*, 3621−3630.

(22) Atwater, H. A.; Polman, A. Plasmonics for Improved Photovoltaic Devices. *Nat. Mater.* **2010**, *9*, 205−213.

(23) Shah, A. A.; Umar, A. A.; Salleh, M. M. Efficient quantum capacitance enhancement in DSSC by gold nanoparticles plasmonic effect. *Electrochim. Acta* **2016**, *195*, 134−142.

(24) Garmaroudi, Z. A.; Mohammadi, M. R. Plasmonic effects of infiltrated silver nanoparticles inside TiO_2 film: Enhanced photovoltaic performance in DSSCs. *J. Am. Ceram. Soc.* **2016**, *99*, 167−173.

(25) Xu, Q.; Liu, F.; Liu, Y.; Meng, W.; Cui, K.; Feng, X.; Zhang, W.; Huang, Y. Aluminum plasmonic nanoparticles enhanced dye sensitized solar cells. *Opt. Express* **2014**, *22*, A301.
(26) Muduli, S.; Game, O.; Dhas, V.; Vijayamohanan, K.; Bogle, K. A.; Valanoor, N.; Ogale, S. B. TiO_2-Au plasmonic nanocomposite for enhanced dye sensitized solar cell (DSSC) performance. *Sol. Energy* **2012**, *86*, 1428−1434.
(27) Dhas, V.; Muduli, S.; Lee, W.; Han, S.-H.; Ogale, S. Enhanced conversion efficiency in dye-sensitized solar cells based on ZnO bifunctional nanoflowers loaded with gold nanoparticles. *Appl. Phys. Lett.* **2008**, *93*, 243108.
(28) Chandiran, A. K.; Abdi-Jalebi, M.; Nazeeruddin, M. K.; Grätzel, M. Analysis of electron transfer properties of ZnO and TiO_2 photoanodes for dye sensitized solar cells. *ACS Nano* **2014**, *8*, 2261−2268.
(29) Rodríguez-Pérez, M.; Canto-Aguilar, E. J.; García-Rodríguez, R.; De Denko, A. T.; Oskam, G.; Osterloh, F. E. Surface photovoltage spectroscopy resolves interfacial charge separation efficiencies in ZnO dye-sensitized solar cells. *J. Phys. Chem. C* **2018**, *122*, 2582−2588.
(30) Idígoras, J.; Burdziński, G.; Karolczak, J.; Kubicki, J.; Oskam, G.; Anta, J. A.; Ziółek, M. The impact of the electrical nature of the metal oxide on the performance in dye-sensitized solar cells: New look at old paradigms. *J. Phys. Chem. C* **2015**, *119*, 3931−3944.
(31) Patwari, J.; Shyamal, S.; Khan, T.; Ghadi, H.; Bhattacharya, C.; Chakrabarti, S.; Pal, S. K. Inversion of activity in DSSC for TiO_2 and ZnO photoanodes depending on the choice of sensitizer and carrier dynamics. *J. Lumin.* **2019**, *207*, 169−176.
(32) Cai, H.; Liang, P.; Hu, Z.; Shi, L.; Yang, X.; Sun, J.; Xu, N.; Wu, J. Enhanced photoelectrochemical activity of ZnO-coated TiO_2 nanotubes and its dependence on ZnO coating thickness. *Nanoscale Res. Lett.* **2016**, *11*, 1−11.
(33) Fabregat-Santiago, F.; Garcia-Belmonte, G.; Mora-Seró, I.; Bisquert, J. Characterization of nanostructured hybrid and organic solar cells by impedance spectroscopy. *Phys. Chem. Chem. Phys.* **2011**, *13*, 9083−9118.
(34) Kalyanasundaram, K. *Dye-Sensitized Solar Cells*; EPFL Press, 2010.
(35) Kakiage, K.; Aoyama, Y.; Yano, T.; Otsuka, T.; Kyomen, T.; Unno, M.; Hanaya, M. An achievement of over 12 percent efficiency in an organic dye sensitized solar cell. *Chem. Commun.* **2014**, *50*, 6379−6381.
(36) Gong, J.; Sumathy, K.; Qiao, Q.; Zhou, Z. Review on dye-sensitized solar cells (DSSCs): Advanced techniques and research trends. *Renewable Sustainable Energy Rev.* **2017**, *68*, 234−246.
(37) Jang, Y. H.; Jang, Y. J.; Kochuveedu, S. T.; Byun, M.; Lin, Z.; Kim, D. H. Plasmonic dye-sensitized solar cells incorporated with Au-TiO_2 nanostructures with tailored configurations. *Nanoscale* **2014**, *6*, 1823−1832.
(38) Erwin, W. R.; Zarick, H. F.; Talbert, E. M.; Bardhan, R. Light trapping in mesoporous solar cells with plasmonic nanostructures. *Energy Environ. Sci.* **2016**, *9*, 1577−1601.
(39) Chander, N.; Khan, A. F.; Thouti, E.; Sardana, S. K.; Chandrasekhar, P. S.; Dutta, V.; Komarala, V. K. Size and concentration effects of gold nanoparticles on optical and electrical properties of plasmonic dye sensitized solar cells. *Sol. Energy* **2014**, *109*, 11−23.
(40) Ng, S.-P.; Lu, X.; Ding, N.; Wu, C.-M. L.; Lee, C.-S. Plasmonic enhanced dye-sensitized solar cells with self-assembly gold-TiO_2@ core-shell nanoislands. *Sol. Energy* **2014**, *99*, 115−125.
(41) Villanueva-Cab, J.; Olalde-Velasco, P.; Romero-Contreras, A.; Zhuo, Z.; Pan, F.; Rodil, S. E.; Yang, W.; Pal, U. Photocharging and band-gap narrowing effects on the performance of plasmonic photoelectrodes in dye-sensitized solar cells. *ACS Appl. Mater. Interfaces* **2018**, *10*, 31374−31383.
(42) Chang, S.; Li, Q.; Xiao, X.; Wong, K. Y.; Chen, T. Enhancement of low energy sunlight harvesting in dye-sensitized solar cells using plasmonic gold nanorods. *Energy Environ. Sci.* **2012**, *5*, 9444−9448.
(43) Mandal, P.; Sharma, S. Progress in plasmonic solar cell efficiency improvement: A status review. *Renewable Sustainable Energy Rev.* **2016**, *65*, 537−552.
(44) Borbón, S.; Lugo, S.; López, I. Fast synthesis of ZnO nanoflowers using a conductively heated sealed-vessel reactor without additives. *Mater. Sci. Semicond. Process.* **2019**, *91*, 310−315.

https://dx.doi.org/10.1021/acsomega.0c00794
ACS Omega 2020, 5, 10977−10986